Soft Matter

PAPER

View Article Online
View Journal | View Issue

Cite this: *Soft Matter*, 2026, **22**, 2038

Interactions of thermochromic liquid crystals with surface-modified PET substrates for thermal sensing applications

Sreenivasan Sreenivasan Narayanan,[a] Lineth Pérez Monsalve,[a] Christina Tang*[b] and Hong Zhao *[a]

Liquid crystals have gained significant attention worldwide for use in digital displays, sensing, smart textures, *etc.* Thermochromic liquid crystals, which respond to temperature, find applications in medical diagnostics and industrial monitoring through temperature sensing and mapping. Here, we deposited a thermochromic cholesteric liquid crystal (CLC) ink on surface-modified polyethylene terephthalate (PET) substrates using doctor blade coating and direct ink writing (DIW) methods, enabling its use for monitoring temperature changes in various applications. We investigated the thermochromic responses of the CLC ink films doctor blade-coated at different temperatures and analyzed how the processing temperature influences the surface characteristics, alignment of the liquid crystals, and their thermochromic behavior. Based on these observations, we identified the optimal printing temperature for the DIW process. We elucidated the interaction of CLCs with surface treatment, such as hydrophobic and hydrophilic coatings, and how they affect the spreading behavior and thermochromic response of CLCs printed on the coated PET substrates. The results demonstrate that the hydrophobic coating intensifies the temperature response of the CLC by drastically reducing ink spreading. This result is supported by the wetting studies of the CLC ink on various substrates and the wetting envelopes, which are developed to predict the contact angles of the ink on these surfaces. Direct ink writing of liquid crystals at elevated temperatures together with the surface treatment of substrates provides a facile way to pattern the liquid crystals with desirable alignment and robust thermochromic performance for temperature sensing applications.

Received 1st December 2025,
Accepted 4th February 2026

DOI: 10.1039/d5sm01182e

rsc.li/soft-matter-journal

Introduction

The distinct phase transitions and thermal characteristics of liquid crystals make them valuable for a variety of applications. Liquid crystals (LCs) are frequently utilized in the production of liquid crystal display (LCD) screens for watches, televisions, and computers. These devices can be precisely controlled because they can modify light in response to electric fields or temperature. Because of their sensitivity to environmental changes, LCs are used in sensors,[1] smart fabrics,[2] and thermochromic coatings[3] in addition to digital displays. Particularly, cholesteric liquid crystals (CLCs) display thermochromic activity, whereby the temperature-induced pitch shift of their chiral nematic phase results in observable color shifts from blue (~450 nm) to red (~760 nm).[4] CLCs become isotropic and cease to reflect visible light above the mesophase transition, but at lower temperatures, the pitch may lengthen to the point that reflection moves outside of the visual spectrum, giving the material an opaque appearance.[4] This thermochromic response facilitates temperature mapping and thermal sensing in the technical and medical domains and is controlled by variables such as transition temperature and phase change enthalpy.[4,5]

Liquid crystals are anisotropic, meaning their behavior changes depending on the orientation and assembly of the liquid crystal molecules. If the molecules are randomly arranged, these properties above become inconsistent or unusable. However, when the molecules are uniformly aligned, their behavior can be controlled and predicted.[6] Controlling liquid crystal (LC) alignment is essential in both scientific and technical applications, with researchers focusing on parameters like the pretilt angle and anchoring strength.[7,8] Conventional alignment techniques include the use of rubbed polyimide layers and surfactants such as silane and lecithin,[9]

[a] *Department of Mechanical and Nuclear Engineering, Virginia Commonwealth University, 70S Madison Street, Richmond, VA, 23220, USA. E-mail: hzhao2@vcu.edu; Tel: +804-827-7025*
[b] *Department of Chemical and Life Science Engineering, Virginia Commonwealth University, 601 West Main St., Richmond, VA, 23284-3028, USA. E-mail: ctang2@vcu.edu; Tel: +804-827-1917*

controlled silicon monoxide film deposition,[10] and flow-induced alignment.[11,12] Traditional polyimide-based alignment layers require high-temperature processing and multiple steps,[13] prompting the development of spontaneous alignment alternatives. Silver nanowires coated with polystyrene can be modified with alkyl or fluoroalkyl groups to reduce surface energy and enhance LC alignment.[14] Polystyrene films with >60% chavicol content or >25% phenylphenoxymethyl (PPHE) groups support stable vertical alignment even under UV exposure and at elevated temperatures.[15] Cellulose acetate substrates functionalized with LC compounds also provide durable homeotropic alignment.[16] Additionally, the drying state of polyvinyl alcohol (PVA) films significantly influences LC droplet deposition by inkjet printing: fully dried films show poor wetting, fully wet films allow spreading but limited alignment, while partially wet films achieve planar alignment of LC directors due to the interfacial interactions.[11] Mechanical stress is a powerful alignment method for liquid crystal elastomers (LCEs). Uniaxial tensile stress, often applied in a two-step crosslinking process developed by Finkelmann and refined by Bowman, is widely used for strong, directional alignment.[17,18] More recent materials with dynamic covalent bonds allow re-alignment post-curing, increasing processing flexibility.[19] While uniaxial stress results in uniform alignment, multiaxial stretching leads to complex orientations.[20] Compressive stress aligns mesogens perpendicular to force, achieved through direct compression or anisotropic deswelling, particularly in cholesteric LCEs.[21] Shear stress is effective in aligning thermoplastic LCEs during molding, extrusion, and especially 3D printing, where alignment along the print path enables programmable mesogen orientation.[22] This method also aids mesogen alignment in microfluidics[23] and fiber-based techniques like electrospinning and drawing.[24] More complex approaches—such as stamping, crimping, and embossing—combine multiple mechanical stresses to create predefined alignment patterns across surfaces.[25] Collectively, these mechanical stress-based methods provide versatile tools for tailoring LCE orientation across a wide range of material systems and fabrication processes.

Using the direct ink writing (DIW) technique to create liquid crystal elastomers (LCEs) has unlocked new possibilities for developing materials that respond to external stimuli in programmable ways while also achieving complex 3D shapes. This approach offers designers a high degree of flexibility—not only in shaping the final object but also in precisely controlling how the liquid crystal molecules are aligned.[26] This combination of structural design and molecular orientation enables the creation of LCEs with tailored, responsive behaviors suited for advanced applications. During the DIW process, shear force facilitates aligning the LCE molecules, which is essential for achieving the desired properties in LCEs.[27] For DIW printing of LCEs, parameters like printing speed, temperature, nozzle size, and the gap between the nozzle and print bed play a crucial role—not only in determining the print resolution and shape accuracy but also in controlling mesogen alignment, which directly affects the responsiveness of the printed LCEs to external stimuli.[28–30] As the temperature increases, the viscosity of the LCE ink decreases, allowing easier flow through the nozzle with less pressure. However, lower temperatures can enhance the ink's shear-thinning behavior, which is important for achieving high-resolution printed structures. Studies have also shown that printing LCEs within their mesophase—rather than in the isotropic phase—leads to better alignment of mesogens along the print direction, resulting in a higher degree of molecular order.[30] To optimize flow and alignment, oligomeric LCE inks are typically printed 10–20 °C below their nematic–isotropic transition temperature.[26,31] Additionally, a biphenyl-based LC polymer ink can be printed in its isotropic state at 200 °C onto a cooler surface (10 °C), where the resulting temperature gradient induces mesogen alignment and an orientation gradient.[32] Although DIW has been utilized to print LCEs with controlled alignment, it has not been demonstrated in printing CLCs, especially when considering interactions with substrates.

The main focus of this work is to examine the effects of hydrophilic and hydrophobic polymer coatings on the CLC ink–substrate interactions as well as to develop the DIW process of the CLC ink with desirable thermochromic performance on various substrates. In particular, we investigated how processing temperature affects the CLC alignment and deposition, and how the surface energy of the substrate treatment influences the CLC wettability and optical responsiveness. We determined the ideal printing temperature based on the roughness and the thermochromic analysis of the CLC films created at various temperatures. During the printing process, the alignment of the CLC ink is promoted through shear-induced and thermally-driven alignment mechanisms. We then printed the CLC ink on coated and uncoated PET substrates. To evaluate the effect of surface coatings on the CLC ink, we studied the spreading behavior of the ink and its thermochromic responses. From these studies, we concluded that the hydrophobic coating on the substrates limited the spreading and resulted in improved thermochromic performance in the reflection light intensity.

Experimental

Materials

Cholesteryl oleyl carbonate (COC, $C_{46}H_{80}O_3$, MW – 681.13 g mol^{-1}, $T_{SA^*–N^*} \sim 20$ °C) was purchased from Sigma Aldrich. Cholesteryl nonanoate also known as cholesteryl pelargonate (CP, $C_{36}H_{62}O_2$, MW – 526.89 g mol^{-1}, $T_{SA^*–N^*} \sim 80$ °C) and cholesteryl benzoate (CB, $C_{34}H_{50}O_2$, 98% purity, MW – 490.76 g mol^{-1}, $T_{SA^*–N^*} \sim 150$ °C) were acquired from Thermo Fisher Scientific. Poly(vinyl alcohol) (MW 9000–10 000 g mol^{-1}, 80% hydrolyzed) and NeverWet solution (auto interior liquid repelling treatment) were purchased from Sigma Aldrich and Rust-Oleum Corporation. Polyethylene terephthalate (PET) films (MELINEX ST505) with a thickness of 125 μm were acquired from TEKRA, a division of EIS. The spray paint used to coat one side of the PET film is Krylon All-In-One Paint + Primer, matte black.

Cholesteric liquid crystal ink preparation

The formulation for the preparation of the CLC ink consists of 30% COC, 60% CP and 10% CB.[33] This ternary mixture was combined under ambient conditions. To ensure thorough blending, the components underwent heating in an oil bath at 90 °C for a duration of 15 minutes, allowing them to fully melt. Following the melting process, the resultant blends exhibited clarity and macroscopic uniformity. Subsequently, the liquid crystal formulation was cooled to ambient conditions before further utilization.

Substrate treatment

To provide a black background for the PET substrates and to enhance the chromic contrast with the CLC ink, we spray-painted one side of the PET with matte black paint. A plasma cleaner (PDC-001-HP) is utilized for cleaning the other side of the substrates, by removing organic contaminants, introducing radicals onto the surface, increasing the surface energy of the material, and rendering the substrates more wettable. This enhancement in surface wettability facilitates the uniform coating of PVA/NeverWet during air spraying. The substrates were plasma treated for 5 minutes using a RF power of 45 W. PVA/NeverWet coating on the substrates is achieved by employing the air spraying method utilizing compressed air to atomize PVA/NeverWet solution into tiny droplets to deposit onto the substrates. The spray gun, equipped with a 0.3 mm diameter nozzle, is connected to an air compressor, and the distance between the nozzle and the substrate was maintained at 20 cm. A PVA solution of 10 wt% was used for air spraying. The quantity used for spraying was approximately 3 mL for both solutions, and the air pressure was maintained at 34 psi. The coated substrates were then dried in an oven at 50 °C for one hour to complete the drying process. To confirm the coating chemistry, we performed attenuated total reflection Fourier transform infrared (ATR-FTIR) spectroscopy using a Nicolet iS50 FT-IR spectrometer at room temperature.

CLC ink film coating

CLC ink films were coated on the PET substrates at various temperatures using an automatic film coater (MSK-AFA-III Automatic Thick film Coater). A doctor blade is employed to spread the CLC material across the substrate, and the gap between the blade and the substrate was maintained at 200 μm, and the coating was performed at a speed of 6 mm s^{-1}.

3D printing

Printing of the CLC ink on various substrates was carried out using a 3D printer, the 3D Bioplotter by EnvisionTEC. The fluid dispensing nozzle had a diameter of 200 μm and was used to print a single layer of CLC lines. The printing pressure was maintained at 0.5 bar, and the ink was heated at 70 °C.

Characterization

The morphologies of the PET substrates were observed using a field emission scanning electron microscope (FE-SEM, HITACHI, SU-70) operating at 5 kV. A goniometer (OCA 15, DataPhysics) and a rheometer (MCR 301, Anton Paar) were used to study the wetting behavior on the substrates and the rheology of the CLC ink, respectively. The roughness characteristics of the coated CLC films were analyzed using an optical microscope of Nikon Eclipse LV100D at room temperature. Details about the roughness calculation are provided in the SI.

The CLC films and printed patterns were characterized after they cooled down to room temperature. Their thermochromic behavior was analyzed using a camera setup with a Peltier plate connected to a water cooler. A Teledyne FLIR color camera (Blackfly S, 12.0 MP resolution) was used, and images of the samples at different temperatures were collected using the SpinView FLIR FL3 software under an exposure setting of 3000. To analyze the color changes of the CLC, the samples were placed on a Peltier plate, the temperature of which was tuned by a temperature controller. A flat probe thermocouple was attached directly to the samples to accurately measure their temperature. An in-house python program was developed to analyze these images to extract the Red, Green, and Blue (RGB) and $L^*a^*b^*$ data for each pixel. The reported RGB and $L^*a^*b^*$ are the average values of the pixels within the selected region of interest.

Results and discussion

The schematic representation of the experiment is shown in Fig. 1. Surface treatment of the substrates was performed using an air spraying technique. Before coating the substrates, we plasma-treated them to enhance wettability, ensuring a uniform coating during the air-spraying process. To estimate the coating thicknesses of PVA and NeverWet, the same spraying conditions were replicated on silicon wafers. We examined the cross-sections using SEM and found that the thicknesses of the PVA and NeverWet coatings were about 9.91 μm and 14.15 μm, respectively, as shown in Fig. S1 in the SI. We conducted FTIR characterization of the PVA-coated and NeverWet-coated PET substrates. The FTIR spectra indicate consistent chemical compositions on both surface coatings (as shown in Fig. S2). The thermochromic behavior of the CLC samples was characterized based on image analysis, using a camera setup and a Peltier plate with a water cooler to stabilize the sample temperature.

Rheology characterization of the CLC ink

Ink rheology, such as viscosity, storage modulus and loss modulus, plays a crucial role in determining ink printability and maintaining the integrity of the printed patterns. To investigate the shear thinning characteristics of the developed ink, rheological tests were performed at various temperatures, including room temperature (RT), 40 °C, 55 °C, 70 °C, and 90 °C. In these tests, the strain rate swept from 0.1 to 100 s^{-1}. As shown in Fig. 2a, the ink exhibited a clear decrease in viscosity with increasing shear rate at all tested temperatures except at 90 °C, confirming its non-Newtonian, shear thinning nature.

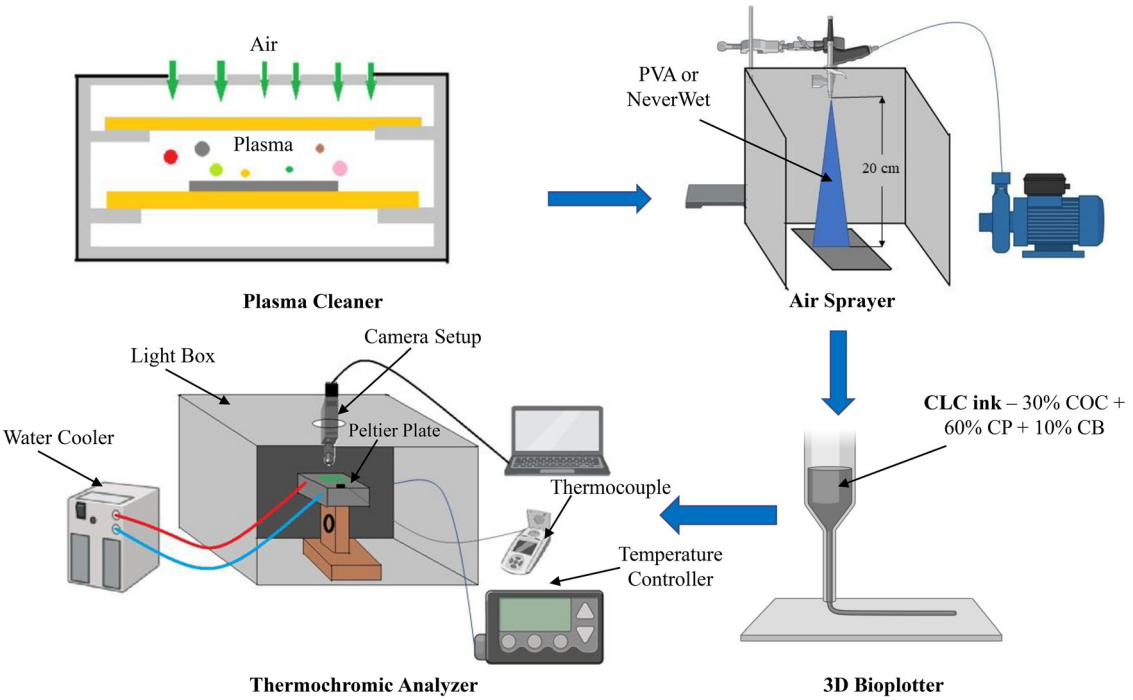

Fig. 1 Schematic representation of the experiment including substrate treatment, 3D printing and image-based thermochromic analysis.

This behavior is beneficial for the extrusion-based printing process as well as film coating applications because the ink remains viscous at rest (preventing unwanted flow or dripping), yet flows easily when shear is applied—facilitating smooth, uniform deposition.

Viscosity as a function of temperature was measured at a constant strain rate of 10 s^{-1}, with the temperature ramped from 22 °C to 90 °C at a rate of 1 °C min^{-1}. From Fig. S3, the viscosity–temperature profile of the CLC ink shows a clear decrease in viscosity with increasing temperature, consistent with the typical behavior of polymeric or liquid crystal-based inks, where thermal energy weakens intermolecular interactions and promotes easier flow. Two distinct phase transitions are evident: the smectic to nematic transition around 36 °C, where viscosity drops as the highly ordered smectic phase shifts to the less-ordered nematic phase, and the nematic to isotropic transition near 75 °C, marked by a further drop in viscosity as the system loses orientational order entirely. The viscosity exhibits a noticeable hump near the smectic–nematic and nematic–isotropic transitions, which likely arises from enhanced molecular fluctuations and the gradual slowing of orientational relaxation as the system approaches these phase boundaries. In these regions, transient defect formation and competing molecular order temporarily impede molecular motion, leading to an increase in viscosity. Similar viscosity anomalies have been experimentally observed near the nematic–isotropic transition and have been attributed to changes in molecular dynamics occurring in the liquid crystal

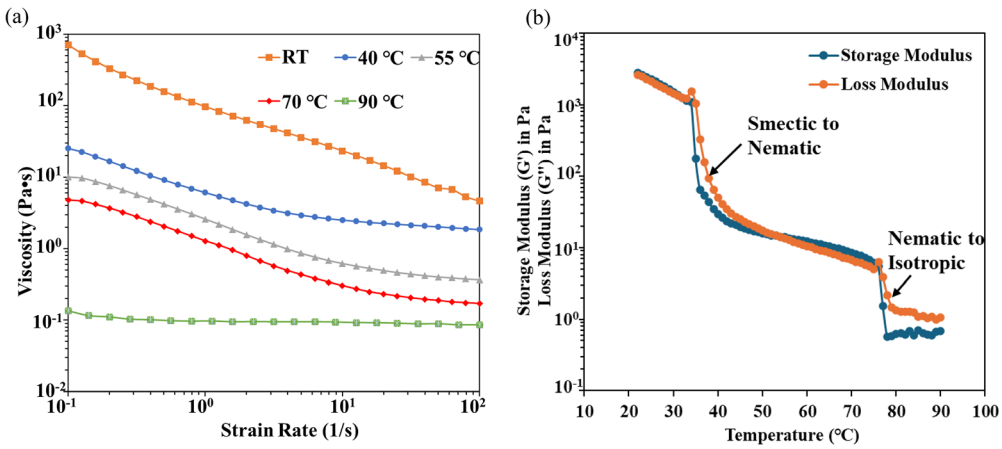

Fig. 2 (a) CLC ink viscosity at RT, 40 °C, 55 °C, 70 °C and 90 °C; (b) temperature sweep of the storage modulus and loss modulus of the CLC ink.

systems.[34,35] Although the data were collected at a constant shear rate, the steep decline in viscosity across these transitions reflects enhanced molecular mobility and flowability, supporting the material's suitability for temperature-controlled printing applications.

To further investigate the viscoelastic behavior of the CLC ink with respect to temperature, rheological modulus measurements were carried out at a constant strain of 1% and a frequency of 10 rad s^{-1}, with the temperature ramped from 22 °C to 90 °C. The storage modulus (G') indicates the elastic behavior of the material, showing how much energy it can store when subjected to deformation, whereas the loss modulus (G'') represents the viscous behavior, reflecting the amount of energy lost as heat during deformation. Higher G' values indicate solid-like behavior, whereas higher G″ values signify liquid-like behavior. At room temperature, as shown in Fig. 2b, both G' and G'' are relatively high (around 3000 Pa), indicating that the CLC ink exhibits a viscoelastic, solid–liquid hybrid nature. Notable drops in both moduli are observed around 36 °C and 75 °C, corresponding to phase transitions: from smectic to nematic at approximately 36 °C, and from nematic to isotropic near 75 °C. Beyond 75 °C, both G' and G'' stabilize at low values, with G''/G' approaching about 2, indicating a predominantly liquid-like behavior.

Study of CLC ink films created at different temperatures

Since the CLC molecular arrangement is directly dependent on the temperature (Fig. 2b), the processing temperature will certainly affect the alignment of the CLC molecules. On the other hand, as described earlier, viscosity decreases with rising temperatures. In order to elucidate the effect of processing temperature on the shear-induced alignment, CLC films were fabricated on a PET substrate using an automatic film coater at different temperatures to investigate their surface roughness and thermochromic properties. We selected five temperatures – 40 °C, 55 °C, 70 °C, 90 °C and 120 °C – for our study based on

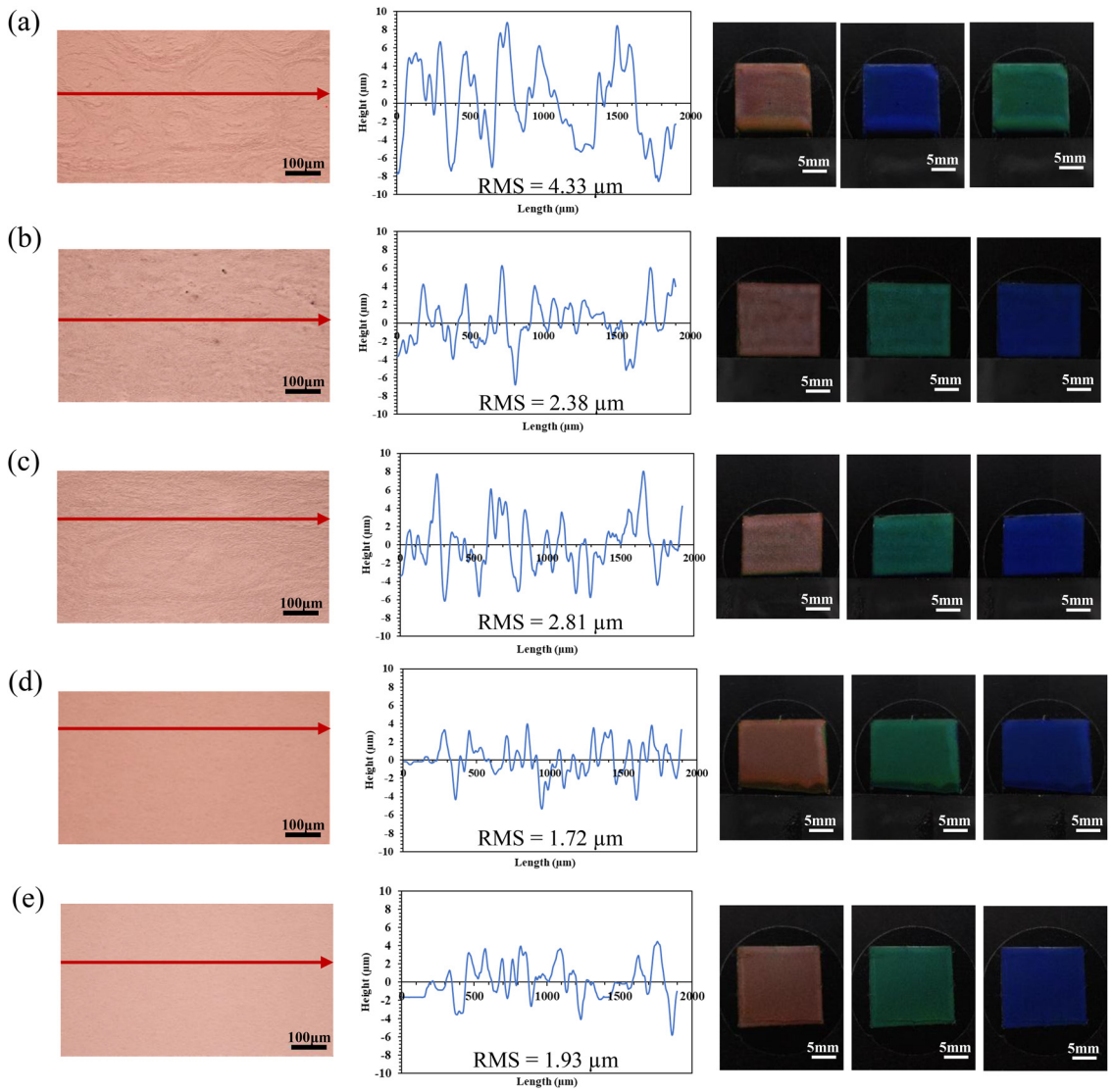

Fig. 3 Surface characteristics and thermochromic behavior of films created at (a) 40 °C; (b) 55 °C; (c) 70 °C; (d) 90 °C; and (e) 120 °C.

specific considerations. Coating at room temperature leads to poor film quality with a very rough surface. We started from a coating temperature of 40 °C, which is also close to the onset of the smectic to nematic phase transition. Rheology data show that phase transitions occur near 36 °C and 75 °C, which agrees well with the transition temperatures measured by differential scanning calorimetry (DSC) (36.1 ± 0.2 °C and 75.2 ± 2.3 °C), as shown in Fig. S4. Therefore, we chose to study films produced at an intermediate temperature, 55 °C, where the ink exhibits a nematic phase. The 70 °C setting represents the onset of transition from the nematic to isotropic phase, making it a practical choice for studying CLC film formation. At 90 °C, the viscosity of the CLC ink significantly decreases, and it behaves as an isotropic liquid; hence, we selected this temperature for our study. At 120 °C, we chose to study how the CLC ink behaves at a higher temperature. Considering all these factors, these five temperatures were selected for our investigation of CLC films.

We used an automatic film coater to create films at these temperatures, maintaining a gap of approximately 200 μm between the doctor blade and the PET substrate. The speed of the automatic film coater was set to 6 mm s^{-1}, ensuring a controlled and consistent application of the CLC ink onto the substrate. The thermochromic response of the CLC films was examined using a camera setup integrated with a Peltier plate, where the film samples were placed. Film specimens, each measuring 1.6 cm × 1.4 cm, were cut and secured onto the Peltier plate using carbon tape. The temperature of the Peltier plate was tuned through a temperature controller, while a digital thermocouple—positioned on the substrate near the sample—was used to monitor the actual sample temperature. The temperature was gradually raised in 0.5 °C increments from 32 °C to 40.5 °C, with each step held for five minutes to ensure uniform heat transfer and allow the sample to reach thermal equilibrium. Fig. 3 shows the optical characterization of the surface topography of the CLC films coated at different temperatures, as well as the thermochromic behavior of the films. Initial observations of the films indicate that the temperature during CLC film fabrication significantly influences their surface morphology. Films produced at 40 °C show largest roughness, likely due to limited ink flow and inadequate leveling. In contrast, the film coated at 90 °C and 120 °C demonstrates a much smoother and more uniform surface. This observation is further supported by the surface roughness analysis conducted using optical microscopy. As shown in Fig. 3, the film coated at 40 °C exhibits the highest roughness compared to films coated at elevated temperatures. The root-mean-square (RMS) roughness value for the film created at 40 °C is 4.33 μm, whereas films coated at 55 °C and 70 °C show reduced RMS values of 2.38 μm and 2.81 μm, respectively. Notably, the films prepared at 90 °C and 120 °C have even lower RMS values of 1.72 μm and 1.93 μm, respectively. This decrease in surface roughness at higher temperatures is likely due to the reduced viscosity of the CLC ink, which promotes improved spreading and self-leveling. These findings underscore the critical role of processing temperature in optimizing film formation and achieving favorable surface qualities for thermochromic applications. Fig. 3 also illustrates the thermochromic behavior of the films, showing distinct peak colors of red, green, and blue at 36.3 °C, 37.3 °C, and 38.3 °C, respectively. Films fabricated at 90 °C and 120 °C exhibit a visually more uniform color distribution across their surfaces, reflecting a smoother and more homogeneous structure.

The variation in surface roughness of the films at different coating temperatures appears primarily at the macro/microscopic scale, with viscosity playing a vital role in this variation. However, at the molecular level, significant changes occur in the molecular arrangement during both the film formation and concurrent thermal activation. During the fabrication process, we use an automatic doctor blade coater, which applies shear force *via* its blade as it spreads the CLC ink across the substrate. As the substrate is placed on the platform heated to elevated temperatures, thermally-driven alignment initiates in the CLC ink coated on the substrate, leading to polydomains of CLC molecules in the nematic phase. On the other hand, shear force tends to align the CLC molecules along the coating direction. However, this shear-induced alignment is largely limited to the topmost surface layer due to the strongest strain rate beneath the coating blade at the interface,[36] while the thermal energy promotes the alignment of the underlying CLC molecules

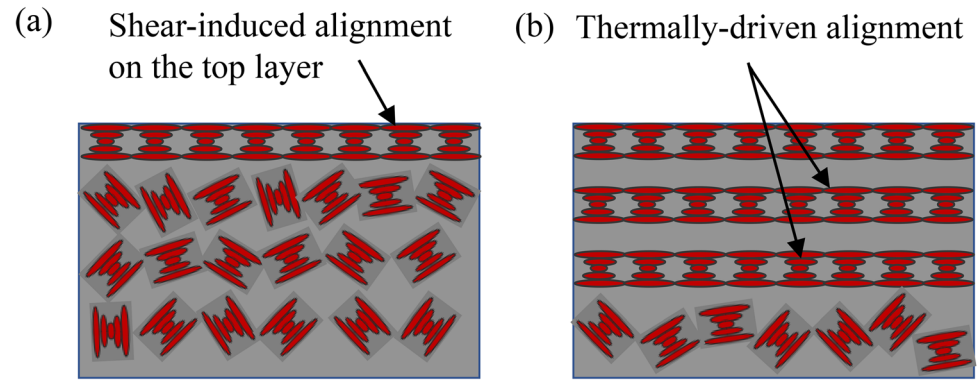

Fig. 4 Alignment of the molecules of the CLC film in the nematic phase, (a) shear-induced alignment; and (b) thermally-driven alignment while anchoring at the top layer.

based on the orientation of the topmost layer, pushing the polydomains towards a more monodomain structure.[37] The schematic diagram of the alignment mechanisms is shown in Fig. 4. As the substrate and the CLC films cool to room temperature, the increase in viscosity helps preserve the molecular alignment, effectively locking the structure. It is worth noting that the temperature variation during characterization only changes the cholesteric pitch rather than the alignment of CLCs due to the relatively low temperatures (up to 40.5 °C). This process of shear-induced and thermally-driven alignment enhances the structural ordering of the CLC molecules in the film. The more uniform this molecular arrangement becomes (*i.e.*, transition from the polydomain to the monodomain), the more effectively the CLC film can exhibit its characteristic thermochromic transition in response to temperature changes. However, at the processing temperatures above 90 °C, the number of aligned layers shall be significantly reduced, primarily due to the transition of the liquid crystal into its isotropic state.

Fig. 5 shows the graphs depicting the RGB and $L^*a^*b^*$ values of the films at different processing temperatures. These graphs are based on the analysis of three samples from each condition, with the plotted values representing the average RGB and $L^*a^*b^*$ values across the three samples. The films on the PET substrate exhibit a distinct color transition from red to blue with increasing temperature, as shown in Fig. 5a. Notably, sharp intensity peaks in the red, green, and blue channels occur at 36.3 °C, 37.3 °C, and 38.3 °C, respectively. It is also evident from the graphs that the film coated at 70 °C exhibits the highest RGB and L^* intensities compared to the other films, while the film coated at 120 °C shows the lowest intensity. The differences in optical intensity across films coated at various temperatures can be explained by the phase transitions of the CLC ink. The film coated at 70 °C demonstrates the highest RGB and L^* intensities likely due to its proximity to the nematic–isotropic transition temperature. At this stage, the liquid crystal molecules have adequate mobility to achieve the more uniform monodomain structure, resulting in enhanced

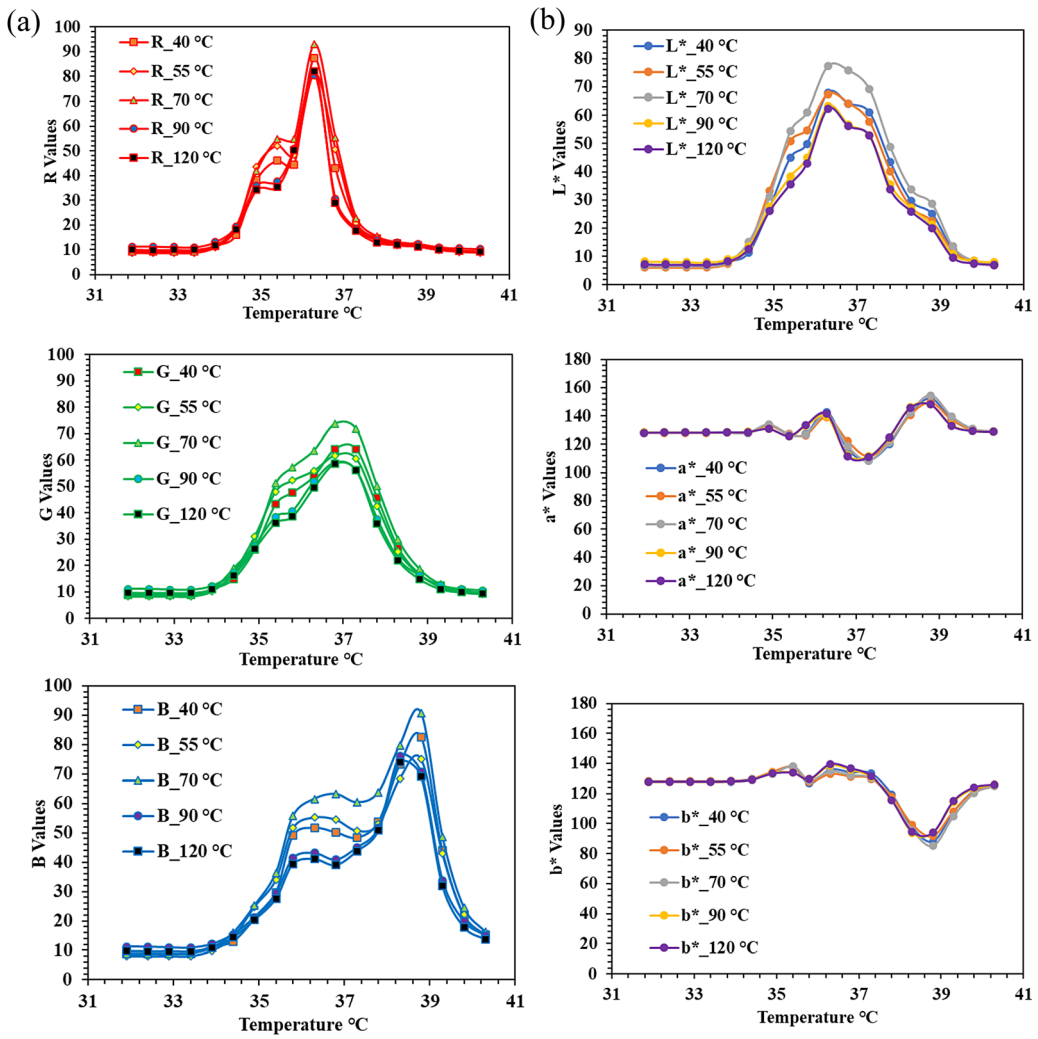

Fig. 5 (a) RGB and (b) $L^*a^*b^*$ of the CLC films created at 40 °C, 55 °C, 70 °C, 90 °C and 120 °C.

Bragg reflection and strong color expression. The films coated at 55 °C and 40 °C show comparable RGB intensities. Although 55 °C is within the nematic phase, the optical response on the films created at this temperature shows a noticeably higher standard deviation (SD) in the RGB values (*i.e.*, ~8–16 of the maximum SDs in Fig. S5) compared to the other coating temperatures. Therefore, although the average value shows lower RGB intensity than the one coated at 40 °C (for the highest peaks of RGB), statistically these two conditions may not be differentiable using the current RGB measurement method. In contrast, films coated at 90 °C and 120 °C display significantly lower RGB intensities as well as L^*. These higher temperatures correspond to the isotropic phase, where molecular order is lost. Consequently, upon cooling, the films exhibit poor reorganization of the cholesteric phase, leading to diminished reflectivity and less distinct color transitions. Moreover, exposure to 120 °C may cause thermal degradation or structural alterations, further reducing optical performance.

In the CIELAB color space, a^* represents the red–green component and b^* represents the yellow–blue component. Changes in these values with temperature indicate a shift in the perceived hue of the sample. As shown in Fig. 5b, it is evident that all films exhibit a consistent chromatic trend, indicating similar color transition behavior across samples regardless of coating temperature. As temperature increases, the a^* values generally decrease, reflecting a reduction in red chromaticity, while b^* values also decline, signifying a shift toward blue hues. This coordinated change in a^* and b^* is characteristic of the thermochromic behavior of CLCs, where the reflected color transitions from red/orange to blue due to temperature-induced changes in helical pitch. The fact that all samples follow the same trajectory highlights the robust and repeatable nature of the CLC ink's color response to temperature, although variations in transition intensity or sharpness may still arise from differences in film quality and molecular alignment resulting from the coating conditions. In this study, the reflection from the printed cholesteric patterns was recorded using a Teledyne FLIR color camera, followed by the extraction of Red, Green, and Blue through imaging analysis. It is selected as the characterization metric because RGB is closely correlated to the human perception of color. Furthermore, it is clearer to compare the RGB of the CLC patterns created under different conditions. The full UV-vis reflection spectrum of the same cholesteric liquid crystal system has been reported in a prior publication,[38] if readers are interested.

Wetting studies on the PET and coated PET substrates

In this study, PVA is selected as a hydrophilic coating due to its unique combination of water solubility, film-forming ability, biocompatibility, and wide range of applications in packaging, surface protection, and medical fields.[39,40] NeverWet, on the other hand, is used as a hydrophobic coating since it strongly repels water, oil, and other solvents.[41] The Owens–Wendt–Rabel–Kaelble (OWRK) model has been employed to measure the surface energy of various substrates (*i.e.*, PET, PVA and NeverWet-coated PET). The OWRK model assumes that the surface free energy has polar and dispersive components and two different types of interactions take place at the solid–liquid interface.[42] The detailed OWRK model is provided in the SI.

The solvents used for the wettability studies were formamide, ethylene glycol, and diiodomethane. The contact angles were measured under ambient conditions at a room temperature of 22 ± 1 °C and RH 34 ± 1% using the sessile drop method. To determine the surface energy of the PET substrate, we measured the contact angles of the three testing liquids on the PET surface. Fig. S6 shows the contact angle results of the solvents on the PET substrates. By applying the measured contact angles to the OWRK model, we calculated the total surface free energy of the PET substrate to be 42.18 mN m^{-1}, with the dispersive and polar components being 40.85 mN m^{-1} and 1.33 mN m^{-1}, respectively. Based on the calculated surface energy of PET, we developed a wetting envelope incorporating contact angle contours as shown in Fig. 6a.

Following similar procedures, we measured the contact angles of the three testing liquids on the PVA-coated and NeverWet-coated PET substrates, as shown in Fig. S7 and S8. The total surface free energy of the PVA-coated PET was determined to be 46.37 mN m^{-1} with the dispersive and polar components of 38.22 mN m^{-1} and 8.14 mN m^{-1}, respectively. For the NeverWet-coated PET substrate, the total surface free energy is 11.13 mN m^{-1} with the dispersive and polar components of 10.87 mN m^{-1} and 0.26 mN m^{-1}, respectively, reflecting its hydrophobic characteristic. The total surface free energy of the PET film was reported as 43 ± 3 mN m^{-1} (ref. 43), which is close to our measured value (42.18 mN m^{-1}). The total surface free energy of pure PVA is typically reported between 30 and 55 mN m^{-1}, heavily influenced by the degree of hydrolysis and molecular weight.[44,45] Our calculated value is 46.37 mN m^{-1}, which falls well within this reported range. In contrast, the surface free energy of hydrophobic coatings is significantly lower than that of regular polymers like PVA, typically falling between 10 and 25 mN m^{-1},[46] and our calculated value is 11.13 mN m^{-1}, which is also consistent with the literature.

The wetting envelope of a solid surface facilitates the convenient prediction of the wetting behavior for a specific liquid, with a known surface tension, specifically its dispersive (Y_L^D) and polar (Y_L^P) components. The wetting envelopes for both substrates are presented in Fig. 6b and c with the contact angle contours. Compared to the contact angle contours on the PET substrate, the contours shift upwards on the PVA-coated substrate, due to its larger polar component in the surface energy; while they shift towards the origin on the NeverWet-coated substrate (*i.e.*, surface tensions of smaller polar and dispersive components), which means for the same surface tension testing liquid, a higher contact angle will be exhibited on the NeverWet-coated PET substrate. In order to predict the wetting behavior of CLCs on the various substrates used in this study, we need to obtain the two components of the CLC surface tension. However, it is challenging to directly measure the surface tension components of CLCs using the traditional pendant drop method or the sessile drop method, due to the

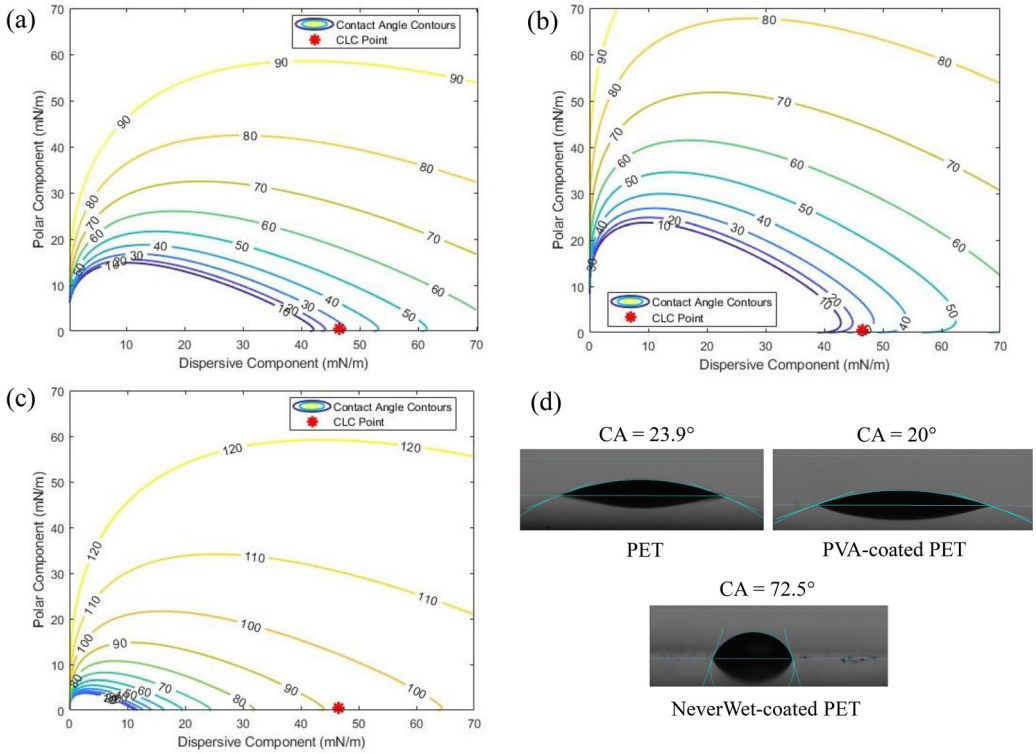

Fig. 6 Wetting envelopes developed for (a) the PET substrate, (b) the PVA coated-PET substrate, (c) the NeverWet coated-PET substrate, and (d) measured CLC contact angles. Wetting envelope shows the contact angle of an arbitrary testing liquid on the substrate, where the *x*-axis and *y*-axis indicate the dispersive component and the polar component of its surface tension, respectively.

highly viscous nature of CLCs at room temperature. Therefore, we calculated the two components of surface energy of the CLC film using the OWRK model and the three testing liquids, which are then utilized as the two components of CLC surface tension for prediction of its wetting behavior on various substrates.

A CLC film was coated onto a PET substrate at 90 °C using the automatic film coater. After cooling down to room temperature, the contact angles of the three testing liquids on these films were measured using a goniometer, as shown in Fig. S9. The total surface energy of the CLC film (*i.e.*, the surface tension of the CLC liquid), is calculated using the OWRK model to be 47.07 mN m^{-1}, with the corresponding dispersive and polar components being 46.49 mN m^{-1} and 0.58 mN m^{-1}, respectively.

The contact angle of the CLC ink on the PET substrate (θ) was then calculated using eqn (1), combining the OWRK model and the Young's equation:

$$\cos\theta = 1 - \frac{2}{Y_L}\left(\sqrt{Y_L^D Y_S^D} + \sqrt{Y_L^P Y_S^P}\right) \quad (1)$$

where Y_L, Y_L^D and Y_L^P represent the CLC surface tension, dispersive and polar components of the CLC surface tension, respectively, and Y_S^D and Y_S^P are the dispersive and polar components of the surface energy of the solid substrates. The calculated CLC contact angles on the PET substrate and the PVA-coated PET substrates are 27.25° and 27.95°, respectively, indicating similar ink wettability on both substrates. This relatively low contact angle can be attributed to the hydrophilic nature of the PVA coating and the PET substrates, which facilitates better wetting of the ink. The predicted contact angle of the CLC ink is 91.62°, suggesting limited wetting on the hydrophobic surface. This behavior is consistent with the hydrophobic nature of the NeverWet coating. While reduced spreading might be a drawback in some printing applications, in this context it can be advantageous by controlling ink spreading and maintaining strong thermochromic responses as discussed later. As shown in Fig. 6a–c, we added the datapoints of the CLC ink to the wetting envelopes to graphically show the predicted CLC contact angles.

To validate our wetting study and the prediction of the CLC ink contact angles on various substrates, we proceeded to experimentally measure the contact angle of the CLC ink at 70 °C on the same substrates to compare it with the predicted values. Fig. 6d shows the contact angle of the CLC ink on the PET and coated PET substrates. When the CLC ink is deposited on the PET and PVA coated-PET substrates held at 70 °C, it spreads rapidly across the surface of both substrates and exhibits low contact angles (23.9° and 20.0°, respectively) after reaching equilibrium. On the NeverWet coated-PET, the CLC ink exhibits a significantly higher contact angle of around 72.5° after reaching equilibrium. The CLC ink does not spread well on this surface, due to the high hydrophobicity of the NeverWet coating. A surface with high surface energy (such as the PET or

PVA coated-PET) interacts strongly with the CLC ink, causing it to spread out (*i.e.*, wetting). In contrast, a surface with low surface energy (such as NeverWet-coated PET) interacts weakly with the liquid, causing it to bead up. The predicted CLC contact angles from the wetting studies agree fairly well with the experimental results with slightly overestimated contact angles. The discrepancies could be due to the estimation of the surface tension of the CLC ink. Nevertheless, the wetting studies reasonably predicted the trend of the contact angle of the CLC ink on both coated and uncoated PET substrates.

CLC ink printing on uncoated and coated PET substrates

Based on the study of the processing temperature effect on the CLC film formation, coating the CLC ink at elevated temperatures enhances the overall performance, *e.g.*, lower surface roughness and stronger thermochromic responses. Films coated at 90 °C and above exhibited the lowest surface roughness, however, decreased RGB intensities. The film coated at 70 °C showed the highest RGB intensity and L^* values, and moderate surface roughness. Therefore, 70 °C was selected as the printing temperature across all substrates. To facilitate the analysis of CLC ink spreading on the substrates, a series of lines were printed on each substrate. The thermochromic behavior of the samples was then quantified by analyzing the RGB and $L^*a^*b^*$ values of the selected lines using image analysis. Similar to the films, the printed CLC patterns also exhibit molecular alignment during the printing process as shown in Fig. 7. The CLC ink molecules take the nematic phase at 70 °C in the ink reservoir. However, this nematic phase is only limited to short-range polydomains. Due to the shear-thinning behavior of the ink, the shear stress generated during printing induces alignment in the CLC molecules starting from the outermost layer. Since the CLC ink is printed at 70 °C, the thermal energy promotes alignment of the underlying CLC molecules utilizing the orientation of the outermost layer as anchoring sites, likely forming the core–shell structure where the core is the polydomain nematic structure and the shell is the aligned monodomain structure. We estimate the degree of alignment using the dimensionless Weissenberg number Wi, which is the product of CLC characteristic time and maximum strain rate during the printing process. With the large Wi number of about 550, the aligned monodomain structure is dominant in the printed lines.[47] The detailed analysis is provided in the SI. As the printed CLC patterns cool down to room temperature, the increased viscosity facilitates preserving this alignment structure in the CLC strands.

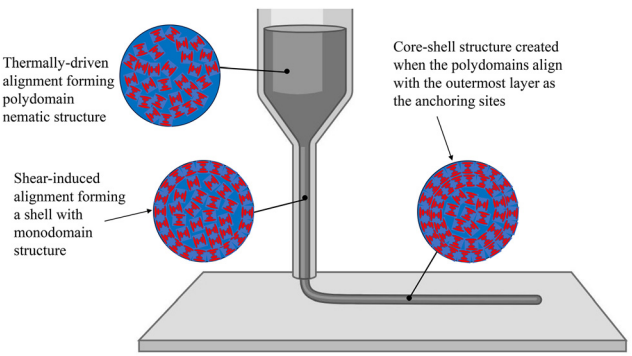

Fig. 7 Schematic diagram representing the alignment of liquid crystals during printing.

We characterized the thermochromic behavior of the printed CLC lines by analyzing their RGB and $L^*a^*b^*$ values. Fig. 8 shows the images illustrating the thermochromic behavior of the printed lines on the PET and coated PET substrates, along with the corresponding RGB and $L^*a^*b^*$ results. The red, green, and blue colors peaked at temperatures of 36.1 ± 0.3 °C, 36.7 ± 0.5 °C, and 38.5 ± 0.2 °C, respectively, on the smooth PET substrate as the printed CLC lines were heated from 32 °C to 41 °C. The PVA-coated PET substrates exhibited the same trend in peak colors as the smooth PET substrates, whereas the NeverWet-coated substrates showed a shift of these color peaks toward lower temperatures.

The intensities of both RGB and L^* are significantly higher for NeverWet-coated substrates compared to PVA-coated and uncoated PET substrates (as shown in Fig. 8). This can be attributed to several factors. NeverWet is a low surface energy coating that resists the spreading of liquids on the substrate. When the CLC ink is printed on the NeverWet-coated PET substrate, it spreads less indicated by the higher ink contact angles. This results in thicker lines (and thicker aligned layers) that reflect more light through stronger optical interference, thereby appearing more saturated and intense in color. Thicker lines offer a greater volume for CLC molecules to establish their stable phases, such as nematic or cholesteric, which can lead to a more consistent and well-formed helical structure. While these thicker regions may take longer to reach thermal equilibrium due to slower heat transfer, it does seem to lead to better alignment[34] and a strong thermochromic response once the temperature stabilizes. In contrast, on the PVA-coated and uncoated PET substrates, the CLC ink spreads more and forms thinner lines, which are more susceptible to anchoring and confinement by the asperities from the substrates, leading to lower RGB intensity. The higher L^* intensity observed on the NeverWet-coated substrates further supports the conclusion that these surfaces facilitate greater light reflection, resulting in a brighter visual appearance.

Another observation is that the color transition on the NeverWet-coated substrates appears to occur at a temperature of about 1 °C lower compared to the other substrates, which can be attributed to the same mechanism discussed earlier: thicker lines tend to have better alignments. Consequently, thicker lines exhibit color transitions at lower temperatures, as the phase transition stabilizes more readily and the helical pitch and molecular order adjust more efficiently. This trend is further supported by the a^* and b^* plots in Fig. 8. On the NeverWet-coated substrate, the a^* and b^* values begin to deviate from their initial states at lower temperatures, implying that the CLC ink starts to show its thermochromic behavior at lower temperatures than that on the PVA-coated or uncoated PET substrates.

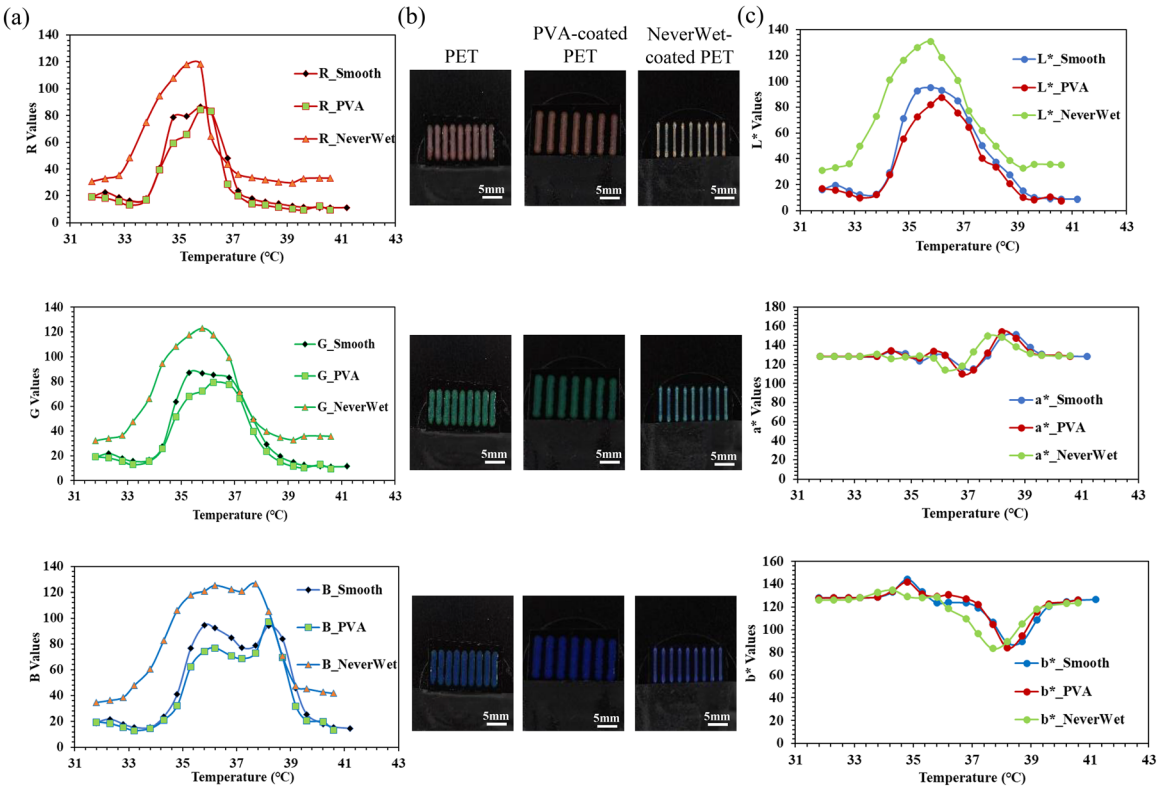

Fig. 8 (a) RGB of printed lines, (b) RGB color transition images, and (c) *L*a*b** of printed lines on the PET uncoated/coated substrates.

Spreading analysis of the CLC ink on the PET and coated-PET substrates

The spreading of the CLC ink on the substrates was measured using ImageJ software. The spreading analysis was conducted during the first heating cycle and after ten heating cycles, with the temperature ranging from 32 °C to 41 °C. For each thermal condition, the widths of five printed lines were measured, and the average line width was calculated. As shown in Fig. 9a, noticeable spreading of the printed lines occurs as the temperature increases, approximately by 57.1% after the first heating cycle. This spreading is primarily attributed to the decrease in the ink viscosity at elevated temperatures and the low contact angle between the CLC ink and the PET substrate. As the contact angle decreases, the ink spreads more readily, resulting in wider lines and rugged line edges (Fig. S11). Fig. 9b shows that after ten heating cycles, the spreading increased to 80.5%. These observations highlight the importance of surface modification using appropriate coatings to manage ink–substrate interactions. By applying coatings that alter surface energy, it is possible to tailor the ink wetting performance and minimize undesirable spreading, thereby improving pattern accuracy and overall print fidelity.

Similar spreading of the printed lines was observed on the PVA coated-PET substrate (Fig. S12) due to the hydrophilic nature of the PVA coating. As shown in Fig. 9a, the spreading of the ink increases by approximately 77.6% as the substrate temperature reaches 40.3 °C after just one heating cycle. The spreading process is also not uniform following a stick-and-spread pattern (*e.g.*, initial smaller spreading followed by larger spreading as temperature increases), which can be attributed to

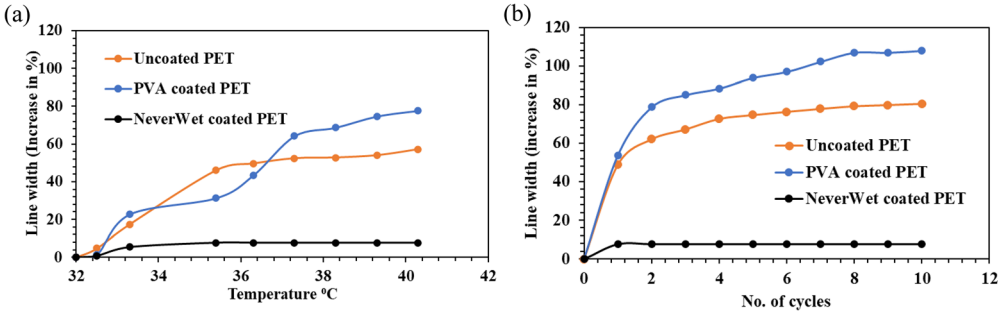

Fig. 9 (a) Spreading analysis for one cycle of heating and (b) ten cycles of heating of printed CLC lines on the PET coated/uncoated substrates.

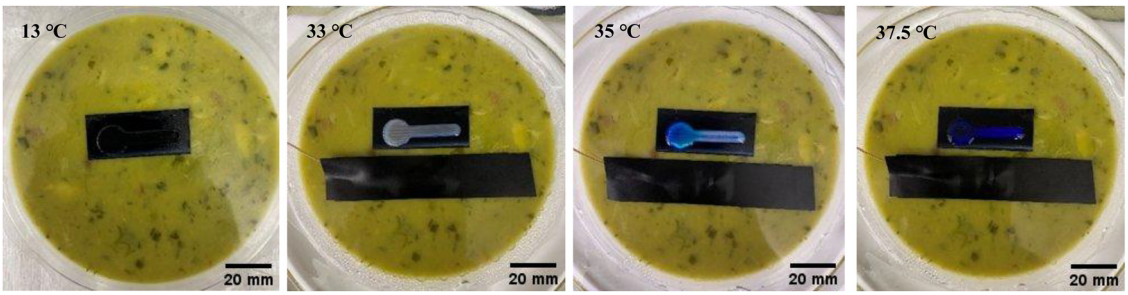

Fig. 10 Color change of a printed CLC temperature indicator on a guacamole package upon temperature variation. Images were captured by a smart phone under ambient lighting conditions.

the surface roughness and textures on the PVA-coated PET substrate. The stronger spreading of the CLC ink on the PVA-coated PET indicated by the crossover in Fig. 9a and subsequent cycles in Fig. 9b is driven by the better wettability of CLCs. The contact angle (wetting) measurements show that the CLC ink has a lower contact angle on PVA-coated PET than that on uncoated PET (Fig. 6d), meaning the ink has a higher affinity toward the PVA surface. As the temperature increases, this favorable ink–substrate interaction becomes more effective, leading to larger line spreading on the PVA-coated substrate. Fig. 9b demonstrates that repeated heating exacerbates the spreading, reaching approximately 108% after ten cycles. Fig. S13 shows the measured line width of the CLC lines on the PVA coated-PET substrate after one cycle and ten cycles of heating.

For substrates coated with NeverWet, the increase in temperature resulted in only minimal changes in the width of the printed lines. This is attributed to the hydrophobic nature of the NeverWet coating, which effectively inhibits ink spreading. This observation aligns with the contact angle measurements, which show significantly higher contact angles for NeverWet coated surfaces compared to other substrates. Based on the image-based analysis as shown in Fig. S14, spreading increased by only 7.8% after the tenth heating cycle—substantially lower than the spreading observed on both the PET and PVA-coated PET substrates. As a result, the printed lines remain well defined, with the original pattern precision and integrity. These findings underscore the benefits of employing hydrophobic surface treatments in CLC sensing applications that demand high print fidelity and stability under thermal cycling.

Demonstration of CLC ink printing on packaging

To demonstrate the practical applicability of the printed CLC patterns for temperature sensing, we printed a thermometer-shaped temperature indicator using the CLC ink onto a black PET sticker coated with NeverWet solution. The sticker was then affixed to the surface of a guacamole package and immersed in a water bath. Fig. 10 illustrates the color transition of the CLC pattern on the package as the guacamole heats up. This demonstration enables us to visually observe the thermal color change of the CLC ink under controlled temperature variations, highlighting its potential use in real-world packaging applications.

Conclusions

In summary, we have studied the deposition of thermochromic cholesteric liquid crystals by doctor blade coating as well as direct ink writing and their interactions with various PET substrates (uncoated, PVA coated, and NeverWet coated). The reflective color on the doctor blade coated films is attributed to the shear-induced alignment of the CLC molecules during deposition combined with the thermally-induced nematic phase of the CLC ink. Higher processing temperatures facilitate smooth CLC film formation due to the reduced viscosity and enhance thermochromic responses thanks to the shear-induced and thermally-driven alignment of CLCs. However, the thermochromic properties may be negatively affected when the processing temperature is too high (*e.g.*, >90 °C). As a result, 70 °C, at which the CLC is still in its nematic phase, but close to the transition temperature to the isotropic phase, has been identified as the optimal coating temperature as well as the printing temperature for the direct ink writing process. Wetting studies on the coated and uncoated PET substrates revealed that the wetting envelopes effectively predicted the wetting behavior of CLC inks. Thermochromic analysis of the printed CLC patterns further confirmed that the hydrophobic coating significantly suppresses liquid crystal spreading resulting in stronger thermochromic responses in the reflection light intensity. It also assists the printed CLC patterns maintaining stability across multiple thermal cycles. Overall, these findings demonstrate the feasibility of 3D printing of thermochromic liquid crystals in various applications for reliable temperature sensing.

Author contributions

Sreenivasan Sreenivasan Narayanan: data curation, formal analysis, methodology, writing – original draft; Lineth Pérez Monsalve: software (programming for RGB extraction); Christina Tang: conceptualization, funding acquisition, methodology, supervision, writing – review and editing; Hong Zhao: conceptualization, funding acquisition, methodology, supervision, writing – review and editing.

Conflicts of interest

There are no conflicts to declare.

Data availability

The supporting data has been provided as part of the supplementary information (SI). Supplementary information: SEM images of PVA coating and NeverWet coating on the PET and its thickness measurements; FTIR spectra of PVA-coated and NeverWet-coated layers; CLC ink viscosity as a function of temperature; DSC characterization of the CLC ink; Standard deviations of Red, Green and Blue of CLC films; Calculation of the surface free energy of a solid surface using OWRK model; Contact angle of solvents on the PET, PVA coated-PET and NeverWet coated-PET substrates; Contact angle of solvents on the CLC film; Analysis of the CLC alignment structure during the DIW process; Images showing spreading of printed CLC lines for one cycle and ten cycles of heating on the PET and coated PET substrates. See DOI: https://doi.org/10.1039/d5sm01182e.

Acknowledgements

This work is funded and supported by the Nonwovens Institute (NWI), North Carolina State University, Raleigh, North Carolina – 22-267SB.

References

1 W. L. Chen, T. Y. Ho, J. W. Huang and C. H. Chen, *Microchem. J.*, 2018, **139**, 339–346.
2 M. Sheng, L. Zhang, D. Wang, M. Li, L. Li, J. L. West and S. Fu, *Dyes Pigm.*, 2018, **158**, 1–11.
3 M. Mostafa, D. M. Agra-Kooijman, K. Perera, A. Adaka, J. L. West and A. Jákli, *Colloid Interface Sci. Commun.*, 2023, **52**, 0–5.
4 I. Sage, *Liq. Cryst.*, 2011, **38**, 1551–1561.
5 Z. C. Yang, N. Wang, Z. Y. Wang, Z. C. Zhang, Y. Wei, L. L. Ma and Y. Q. Lu, *Adv. Opt. Mater.*, 2025, **2500654**, 1–7.
6 P. G. De Gennes and J. Prost, *The Physics of Liquid Crystals*, Oxford University Press, 1993.
7 L. Gao, Y. Zhang, V. Malyarchuk, L. Jia, K. I. Jang, R. Chad Webb, H. Fu, Y. Shi, G. Zhou, L. Shi, D. Shah, X. Huang, B. Xu, C. Yu, Y. Huang and J. A. Rogers, *Nat. Commun.*, 2014, **5**, 1–10.
8 M. J. Shin and D. K. Yoon, *Materials*, 2020, **13**, 1–23.
9 O. Haba, D. Hiratsuka, T. Shiraiwa, N. Funakoshi, H. Awano, T. Koda, T. Takahashi, K. Yonetake, M. Kwak, Y. Momoi, N. Kim, S. Hong, D. Kang and Y. Choi, *Opt. Mater. Express*, 2014, **4**, 934.
10 P. K. Son, J. H. Park, J. C. Kim and T. H. Yoon, *Thin Solid Films*, 2007, **515**, 3102–3106.
11 E. Parry, D. J. Kim, A. A. Castrejón-Pita, S. J. Elston and S. M. Morris, *Opt. Mater.*, 2018, **80**, 71–76.
12 D. J. Gardiner, W. K. Hsiao, S. M. Morris, P. J. W. Hands, T. D. Wilkinson, I. M. Hutchings and H. J. Coles, *Soft Matter*, 2012, **8**, 9977–9980.
13 T. Naing Oo, T. Iwata, M. Kimura and T. Akahane, *Sci. Technol. Adv. Mater.*, 2005, **6**, 149–157.
14 H. Kang, J. S. Park, D. Kang and J. C. Lee, *Polym. Adv. Technol.*, 2009, **20**, 878–886.
15 J. Moon, K. Seo and H. Kang, *Polymers*, 2021, **13**, 819.
16 B. Sivaranjini, R. Mangaiyarkarasi, V. Ganesh and S. Umadevi, *Sci. Rep.*, 2018, **8**, 1–13.
17 J. Zhao, L. Zhang and J. Hu, *Adv. Intell. Syst.*, 2022, **4**, 1–13.
18 R. R. Gadkari, A. Gupta, U. Teke, A. Awadhiya, M. Shahadat, W. Ali, A. Das and R. Alagirusamy, *J. Ind. Eng. Chem.*, 2021, **99**, 214–223.
19 Y. Wu, Y. Yang, X. Qian, Q. Chen, Y. Wei and Y. Ji, *Angew. Chem., Int. Ed.*, 2020, **59**, 4778–4784.
20 C. Ahn, X. Liang and S. Cai, *Extrem. Mech. Lett.*, 2015, **5**, 30–36.
21 R. Kizhakidathazhath, Y. Geng, V. S. R. Jampani, C. Charni, A. Sharma and J. P. F. Lagerwall, *Adv. Funct. Mater.*, 2020, **30**, 1909537.
22 M. O. Saed, C. P. Ambulo, H. Kim, R. De, V. Raval, K. Searles, D. A. Siddiqui, J. M. O. Cue, M. C. Stefan, M. R. Shankar and T. H. Ware, *Adv. Funct. Mater.*, 2019, **29**, 1–9.
23 M. Urbanski, C. G. Reyes, J. Noh, A. Sharma, Y. Geng, V. Subba Rao Jampani and J. P. F. Lagerwall, *J. Phys.: Condens. Matter*, 2017, **29**, 133003.
24 D. J. Roach, C. Yuan, X. Kuang, V. C. F. Li, P. Blake, M. L. Romero, I. Hammel, K. Yu and H. J. Qi, *ACS Appl. Mater. Interfaces*, 2019, **11**, 19514–19521.
25 M. Barnes and R. Verduzco, *Soft Matter*, 2019, **15**, 870–879.
26 M. Chen, M. Gao, L. Bai, H. Zheng, H. J. Qi and K. Zhou, *Adv. Mater.*, 2023, **35**, 1–31.
27 K. M. Herbert, H. E. Fowler, J. M. McCracken, K. R. Schlafmann, J. A. Koch and T. J. White, *Nat. Rev. Mater.*, 2022, **7**, 23–38.
28 L. Ren, B. Li, Y. He, Z. Song, X. Zhou, Q. Liu and L. Ren, *ACS Appl. Mater. Interfaces*, 2020, **12**, 15562–15572.
29 A. Kotikian, R. L. Truby, J. W. Boley, T. J. White and J. A. Lewis, *Adv. Mater.*, 2018, **30**, 1–6.
30 C. P. Ambulo, J. J. Burroughs, J. M. Boothby, H. Kim, M. R. Shankar and T. H. Ware, *ACS Appl. Mater. Interfaces*, 2017, **9**, 37332–37339.
31 Y. Zhao, J. Li, L. Ren, Q. Liu, L. Ren, K. Wang and B. Li, *J. Mater. Res. Technol.*, 2024, **33**, 5683–5691.
32 C. Zhang, X. Lu, G. Fei, Z. Wang, H. Xia and Y. Zhao, *ACS Appl. Mater. Interfaces*, 2019, **11**, 44774–44782.
33 M. W. Williams, J. A. Wimberly, R. M. Stwodah, J. Nguyen, P. A. D'Angelo and C. Tang, *ACS Appl. Polym. Mater.*, 2023, **5**, 3065–3078.
34 R. Kimura, H. Kitakado, T. Yamakado, H. Yoshida and S. Saito, *Chem. Commun.*, 2022, **58**, 2128–2131.
35 R. Shimada, O. Urakawa, T. Inoue and H. Watanabe, *Soft Matter*, 2021, **17**, 6259–6272.
36 W. H. Liang, D. Y. Wu and J. H. Cao, *Phys. Fluids*, 2022, **34**, 073103.
37 A. Ng, R. Telles, K. S. Riley, J. A. Lewis, C. C. Cook, E. Lee and S. Yang, *Adv. Mater.*, 2025, **37**, 1–11.
38 S. L. Levit, J. Nguyen, N. P. Hattrup, B. E. Rabatin, R. Stwodah, C. L. Vasey, M. P. Zeevi, M. Gillard, P. A. D'Angelo, K. W. Swana and C. Tang, *ACS Omega*, 2020, **5**, 7149–7157.
39 L. Rahman and J. Goswami, *J. Packag. Technol. Res.*, 2023, **7**, 1–10.
40 N. Ben Halima, *RSC Adv.*, 2016, **6**, 39823–39832.

41 W. Zhang, D. Wang, Z. Sun, J. Song and X. Deng, *Chem. Soc. Rev.*, 2021, **50**, 4031–4061.
42 K. Y. Law and H. Zhao, *Surface Wetting: Characterization, Contact angle, and Fundamentals*, Springer, 2016, 41.
43 R. Cueff, G. Baud, J. P. Besse, M. Jacquet and M. Benmalek, *J. Adhes.*, 1993, **42**, 249–254.
44 E. Olewnik-Kruszkowska, M. Gierszewska, E. Jakubowska, I. Tarach, V. Sedlarik and M. Pummerova, *Polymers*, 2019, **11**, 2093.
45 M. Barbălată-Mândru, D. Serbezeanu, M. Butnaru, C. M. Rîmbu, A. A. Enache and M. Aflori, *Materials*, 2022, **15**, 2493.
46 S. Pan, Q. Hu, Y. Zhao, Q. Wang, Y. Li, Y. Qian and C. He, *Materials*, 2023, **16**, 1–12.
47 R. Telles, A. Kotikian, G. Freychet, M. Zhernenkov, P. Wąsik, B. M. Yavitt, J. L. Barrera, C. C. Cook, R. Pindak, E. C. Davidson and J. A. Lewis, *Proc. Natl. Acad. Sci. U. S. A.*, 2025, **122**, 3.